



Removal of Cr(VI) from aqueous solutions using polymer nanotubes

Sheng Yu¹, Guoming Yuan¹, Hejun Gao^{1,2,*} , and Yunwen Liao^{1,2,*}

¹Chemical Synthesis and Pollution Control Key Laboratory of Sichuan Province, China West Normal University, Nanchong 637000, China

²Institute of Applied Chemistry, China West Normal University, Nanchong 637000, China

Received: 30 April 2019

Accepted: 3 September 2019

Published online:

9 September 2019

© Springer Science+Business Media, LLC, part of Springer Nature 2019

ABSTRACT

The self-assembled polymer nanotubes were obtained by a simple solvothermal method. Its physicochemical properties were characterized by SEM, BET, TGA, FT-IR, XPS, and solid-state ¹³C magnetic resonance. The effects of initial pH, dosage, and coexisting ions were evaluated for its Cr(VI) adsorption performances. The result showed that polymer nanotubes surface had a large number of organic functional groups and porous structures. In 140 mg/L Cr(VI) solution, polymer nanotubes obtained the largest Cr(VI) adsorption capacity of 147.81 mg/g. Adsorption kinetics and isotherms agreed well with the pseudo-second-order and Redlich–Peterson models, respectively. The desorption process showed that the polymer nanotubes were easy to regenerate in strong polarity solution and had a high removal efficiency. Ionic strength played an important role in the adsorption and the adsorption interaction contained electrostatic interaction, reduction, and chelation in this work. The self-assembly method will constitute a highly efficient adsorbent.

Introduction

As we know, most metals are trace elements that people need [1]. However, with the process of industrialization and urbanization, heavy metal emissions have far exceeded the tolerance of the ecosystem. It seriously threatens environmental safety and human health. Among these metals, chromium is one of the most common contaminants [2]. Chromium exists mainly in two forms in water [trivalent chromium Cr(III) and hexavalent chromium Cr(VI)]. Cr(III) is an indispensable trace

element that benefited metabolizing sugar, protein, and fat [3]. Nevertheless, Cr(VI) has been reported to cause cancer, vomiting, diarrhea, kidney, liver damage, skin irritation, and ulcers for humans, which was highly soluble, mobile, and toxic in aqueous media. Therefore, Cr(VI) was listed as one of 16 toxic heavy metals that are harmful to human health [4]. In recent years, the US Environmental Protection Agency (EPA) Guidelines gave a maximum capacity of Cr(VI) in potable water (0.05 mg L⁻¹). In summary, the removal of Cr(VI) from wastewater is an urgent task.

Address correspondence to E-mail: hejun_gao@126.com; iao-yw@163.com

Currently, many methods have been applied to remove Cr(VI) from water, such as photocatalysis, ion exchange, chemical precipitation, electrochemical treatment, and membrane process [5]. However, there are some disadvantages in those methods, which limit their practical application in wastewater treatment, such as uneconomic, toxic sludge, inefficiency, and environmental pollution. While adsorption has the advantages of simple design, environmental friendliness, low cost, high efficiency, and repeatability, it is considered to be a simple and effective way to separate Cr(VI) from aqueous solution [6].

Up to now, numerous different materials have been reported as adsorbents, such as activated carbon [7], clay, metal oxides, silica [8], titanium dioxide [9], graphene materials [10], and polymer [11]. Among these adsorbents, polymers have a high specific surface area [12] and adjustable functional group. The polymer substrates are also used to prepare various complexes (e.g., polymer/carbon [13], polymers/metal [14]). Polymer adsorbents have become a research hotspot. Especially, the porous polymer has unique properties (low skeletal density and high chemical stability). Wu [15] reported that leucoemeraldine-based hybrid porous polyanilines had been synthesized by the Friedel–Crafts reaction of leucoemeraldine and octavinylsilsesquioxane for Cr(VI) removal. However, most porous polymer adsorbents are disordered structures. Notably, there are few reports on self-assembled porous polymer materials obtained by one-step Friedel–Crafts reaction at high temperature and high pressure.

In this work, we prepared porous polymer nanotubes by the one-step method using 2-aminobenzimidazole and *a,a'*-dichloro-*p*-xylene as raw materials. The surface of porous polymer nanotubes was easily regulated by pH due to the functional groups. This work will provide a new efficient way to self-assemble porous polymer adsorbent.

Experimental

Materials

2-Aminobenzimidazole, *a,a'*-dichloro-*p*-xylene, 1,2-dichloroethane, potassium chloride, potassium carbonate, potassium acetate, ferric chloride, and potassium dichromate were purchased from Aladdin

Chemical Reagent Company (Shanghai, China). Ethanol was obtained from Kelong Chemical Reagent Company (Chengdu, China). All reagents are not purified before use, and deionized water was used throughout the experiments.

Preparation of porous polymer nanotubes

Typical methods for the self-assembled porous polymer nanotubes (PNT) are as follows. 2-Aminobenzimidazole (0.3781 g, 2.84 mmol), *a,a'*-dichloro-*p*-xylene (0.9943 g, 5.68 mmol), and FeCl₃ (1.8403 g, 11.36 mmol) were added into 30 mL 1,2-dichloroethane. The mixture was mixed with vigorous stirring. Then, it was heated to 180 °C with 5 °C min⁻¹ under N₂ for 7 h. The polymer was collected by filtration. It was washed with deionized water several times. Then, the polymer was further purified by Soxhlet extraction using ethanol. After drying, the black solid was obtained with a 90% yield. The different molar ratios (*a,a'*-dichloro-*p*-xylene/2-Aminobenzimidazole = 1:2, 1:1, and 2:1) were marked as PNT1, PNT2, and PNT3, respectively.

Characterization of PNT

The morphology and mapping of PNT were investigated by S4800 (SEM, Hitachi Ltd., Japan). Brunauer–Emmett–Teller (BET) was used to calculate the specific surface area and pore-size distribution (version 3.0, Quantachrome Instruments Ltd., USA). STA 449F3 was applied to explore thermogravimetric analyses (TGA, Netzsch Ltd., Germany). The surface groups were measured by FT-IR 5700 (Thermo Nicolet Ltd., USA). PHI-5400 XPS with Mg K α radiation was used to measure the X-ray photoelectron spectroscopy (XPS). The Bruker Avance DSX spectrometer was applied to examine the solid-state ¹³C magnetic resonance (NMR) spectrum.

Batch experiment

The adsorption capacity of PNT was carried out in batch experiment. Typical operation process is as follows. PNT (6 mg) was added into 10 mL of 20 mg/L Cr(VI) solution with stirring at room temperature for 4 h. The mixture solutions were filtered by 0.45 μ m filter. The Cr(VI) concentration was measured by diphenylcarbazide spectrophotometry. The range of pH was 1.5–11 in the pH-effect tests, and

the range of PNT dosage was 0.2–1.0 g/L in dosage-effect tests; the range of Cr(VI) concentrations was 20–140 mg/L in isotherm investigations. The adsorption capacity and removal rate could be calculated by Eqs. (1) and (2), respectively. Dilute HCl and 0.1 M NaOH were used to adjust the initial pH.

$$q_t = (C_0 - C_t)V/m \quad (1)$$

$$\text{Removal (\%)} = (C_0 - C_t) \times 100/C_0 \quad (2)$$

where C_0 (mg L⁻¹) was the initial concentration of the adsorbate in the solution. C_t (mg L⁻¹) is the concentrations of adsorbates at the time t . q_t is the adsorption capacity at the time t . C_t (mg L⁻¹) was the residual concentration in the solution at time t . V (L) was the volume of the solution. m (g) was the mass of the adsorbent.

Desorption

The adsorption–desorption was carried out in five cycles. In each cycle, PNT (6 mg) was added into 10 mL (20 mg L⁻¹, pH = 2) Cr(VI) solution for 4 h. After filtration, the adsorbate was desorbed in regeneration solution (NaOH, C₂H₅OH, CH₃COCH₃) for 4 h. Then, adsorbent was washed with deionized water and reused in the next cycle.

Result and discussions

Characterization

Figure 1 shows the surface microstructure of the PNT. It was a one-dimensional ordered structure (Fig. 1a). It was visible that the one-dimensional ordered structure was a hollow tube. The tube has an outer diameter about 150 nm, an inner diameter about 55 nm, and a length of about 2 μm (Fig. 1b, c). Therefore, the one-dimensional ordered structure was a nanotube. In order to further investigate the nanotube, BET was applied to measure the porous property (Fig. 1d). The nanotube has a specific surface area of about 95 m² g⁻¹. The average pore diameter of 3.79 nm was smaller than the inner diameter (55 nm). It implied the tube was a porous nanotube, which provides a lot of sites for Cr(VI) to be adsorbed.

FT-IR explored the surface functional groups of PNT (Fig. 2). The vibration at 3439 cm⁻¹ was associated with ν[N–H] stretching. It may provide a strong

hydrogen bonding during the self-assembly process [16]. The bands characteristics at 1610, 1488, and 1456 cm⁻¹ were assigned to the self-assembly vibration (ν[C=N] and ν[C=C] stretching). It was obvious stretching vibration at 1170 cm⁻¹ ν[C–N] and 1250–1280 cm⁻¹ ν[C–N]. The strong vibration at 2893 cm⁻¹ and slight stretching vibration at 1500 cm⁻¹ were attributed to ν[CH₂] and benzene ring, respectively [17]. The functional groups played a key role in the self-assembly process.

Decomposition of the samples is shown in Fig. 3. In the 2-Aminobenzimidazole curve, it was only one step of mass loss (~ 207–425 °C). It could be due to the functional groups and carbon skeleton break. The 2-Aminobenzimidazole was almost completely thermally decomposed. PNT showed two steps of weight loss. The first step was shown in ~ 50–420 °C. It was due to the volatile compound (free and bound water molecules) or surface functional groups. Its weight lost 10%. The second step was at ~ 420–770 °C, which was the decomposition of the self-assembling skeleton. It indicated that self-assembly behaviors improve the temperature resistance of the polymer nanotube.

XPS showed the chemical composition of the PNT in Fig. 4. The C1s spectrum was divided into four peaks at 284.7, 285.7, 287.3, and 289 eV. They were the electronic energy of C–C/C=C, sp²C–N, sp³C–N, and π → π*, respectively. π → π* was the special structure of the benzene ring or the delocalized structure. sp²C–N and sp³C–N could be due to the imidazole ring [18]. In N 1s, the band at 399 eV could be disunited into five peaks, which revealed the different energy states of nitrogen (pyridinic N 398.6 eV, pyridonic N 400.2 eV, quaternary N 401.3 eV, oxidized N 403.2 eV, and –NH₂ 400 eV) [19, 20]. Above five energy states content was 31.8%, 14.4%, 27.4%, 6.3% and 20.1%, respectively. The pyrrolic N could provide a pair of electrons for the π-electronic. Only one electron could be denoted to an aromatic system by the pyridinic N. It could coordinate with an empty orbit of an adjacent atom by a free lone pair of electrons. This provides a channel for the surface enrichment of H⁺, implying that the surface of PNT was easily controlled by pH.

To further confirm the chemical structure of PNT, the solid-state ¹³C NMR spectrum is shown in Fig. 5. There are five peaks (37.09, 112.20, 129.23, 137.19, and 154.41 ppm) in the figure. The resonance peak near 37 ppm was assigned to C₅ [21], indicating that PNT

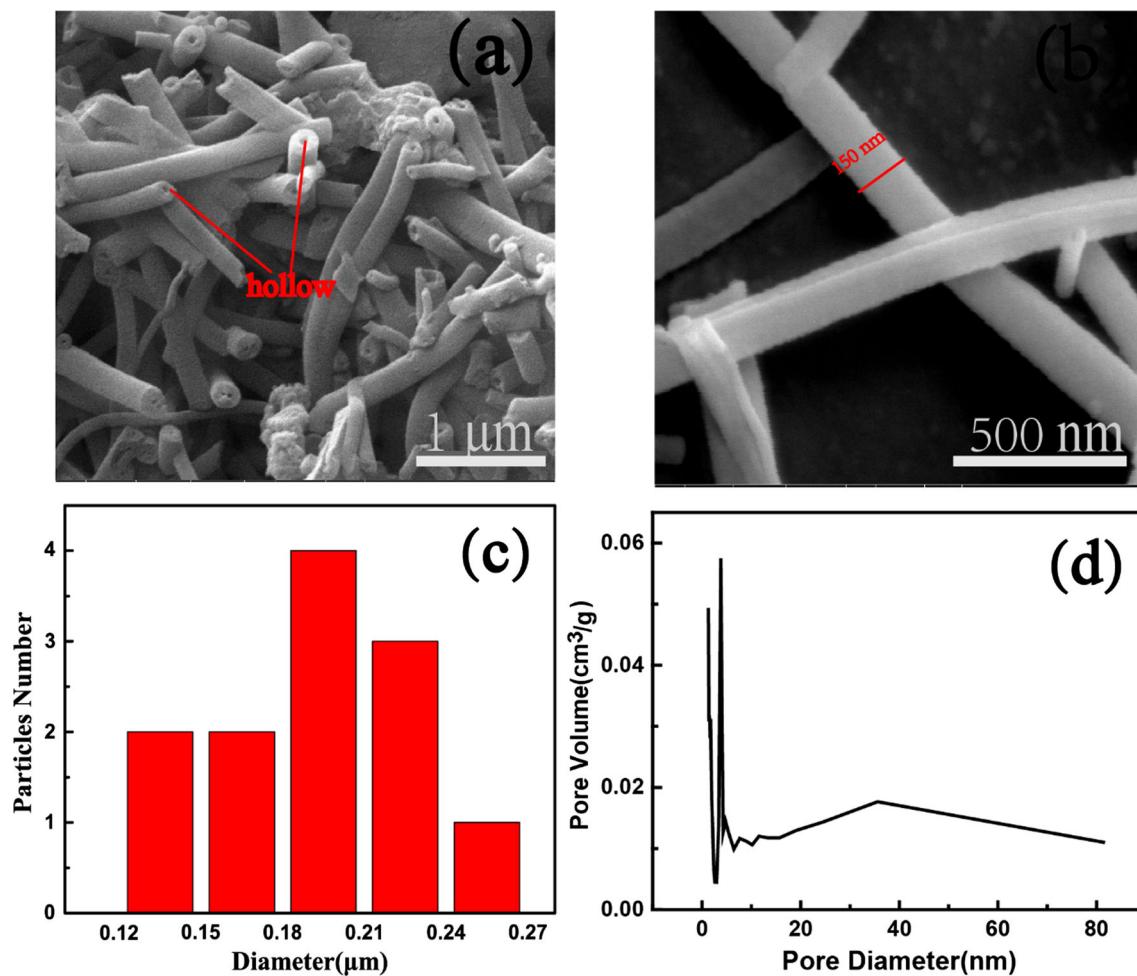


Figure 1 SEM of PNT2 (a, b), nanotubes outer diameter distribution of PNT2 (c) and pore-size distribution of PNT2 (d).

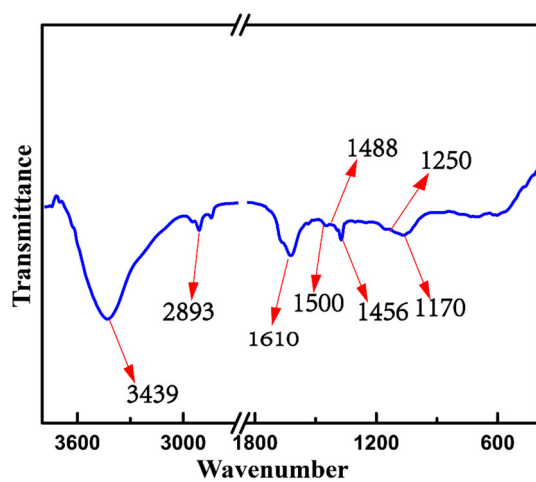


Figure 2 FT-IR of PNT2.

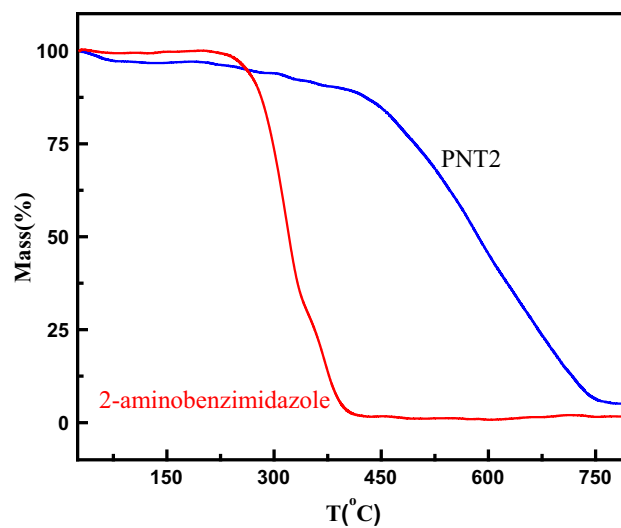


Figure 3 TGA of PNT2 and 2-aminobenzimidazole.

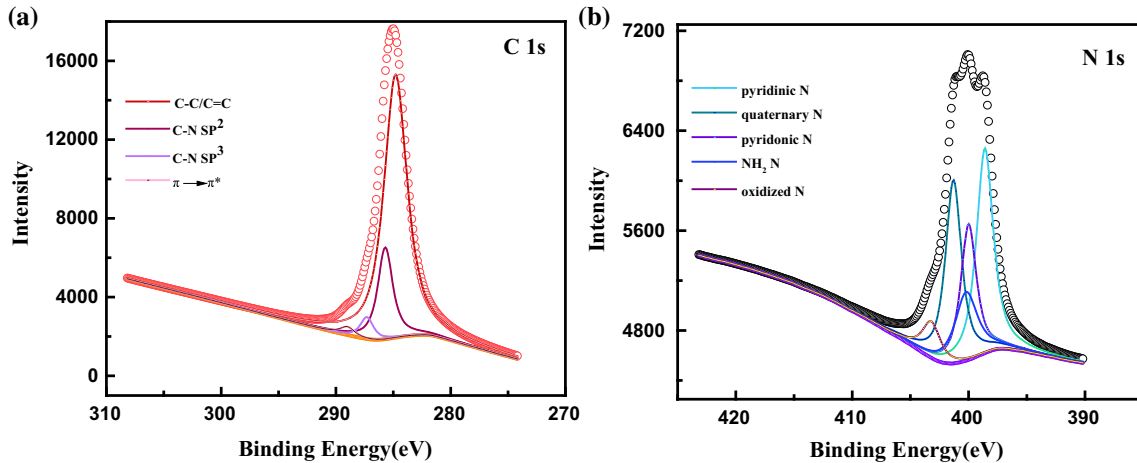


Figure 4 XPS of C 1s (a) and N 1s (b) of PNT2.

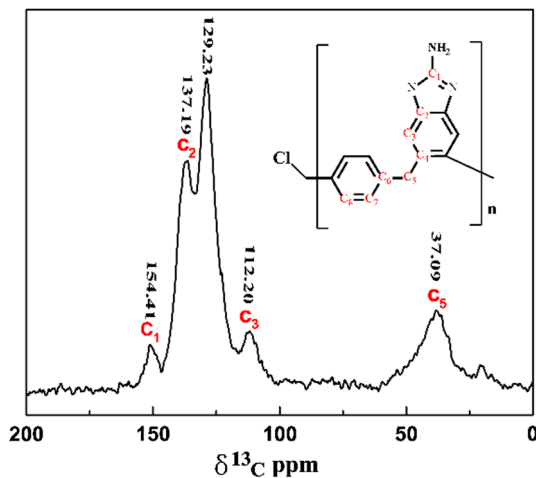


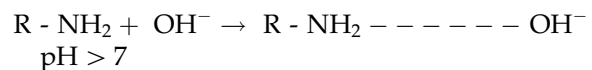
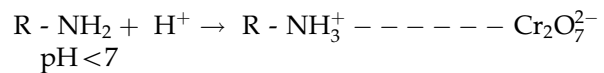
Figure 5 Solid-state ¹³C NMR spectrum of PNT2.

was successfully by the Friedel–Crafts reaction. The peak at 112.20 ppm was due to C₃ [22]. Two bands at 129.23 and 137.19 ppm were attributed to the C₇, C₈ (non-substituted) and the C₂, C₄, and C₆ (substituted aromatic carbon), respectively [23].

Effect of pH

The pH of the contaminant solution is an important factor in exploring the adsorption mechanism. It could affect the ionization of the surface functional groups of PNT and the ionic form of contaminant. The effect of pH on the adsorption of Cr(VI) is illustrated in Fig. 6. The value of *q_t* was gradually decreasing with increasing value of pH. The excellent adsorption capacities of three adsorbents were about at pH = 2.64 (Fig. 6a). The effect of solution pH could

be described as follows. (1) In pH = ~ 2.0–6.0, the form of hexavalent chromium is gradually converted from HCrO₄⁻ to Cr₂O₇²⁻. The adsorption free energies of HCrO₄⁻ and CrO₄²⁻ were about - 2.5–0.6 and - 2.1–0.3 kJ mol⁻¹, respectively. It indicated that HCrO₄⁻ was more easily adsorbed than CrO₄²⁻ [24]. Therefore, the optimal pH value is ~ 2.64 in this work. In pH < 1, H₂CrO₄ was the major formation. Therefore, the electrostatic attraction was weak at pH < 2. The adsorption capacity of PNT at pH = 1.69 was less than that at pH = 2.64 [25]. (2) With the increase in pH value, the groups of -NH₂ and -N- were easy to combine with OH⁻ to cause surface positive charge reduction. It would produce repulsive force to Cr₂O₇²⁻ and reduce the adsorption capacity of PNT (Fig. 6b). It was illustrated in the following equations:



Above all, lower pH (2.64) was beneficial to PNT adsorption of Cr(VI). The adsorption performance of PNT2 was better than that of PNT1 and PNT3. The functional groups of -NH₂ and -N- played an important role in the adsorption process.

Effect of dosage

The amount of PNT was a very vital factor for the actual application process. Figure 7 shows the effect of dosage on the adsorption capacity and removal

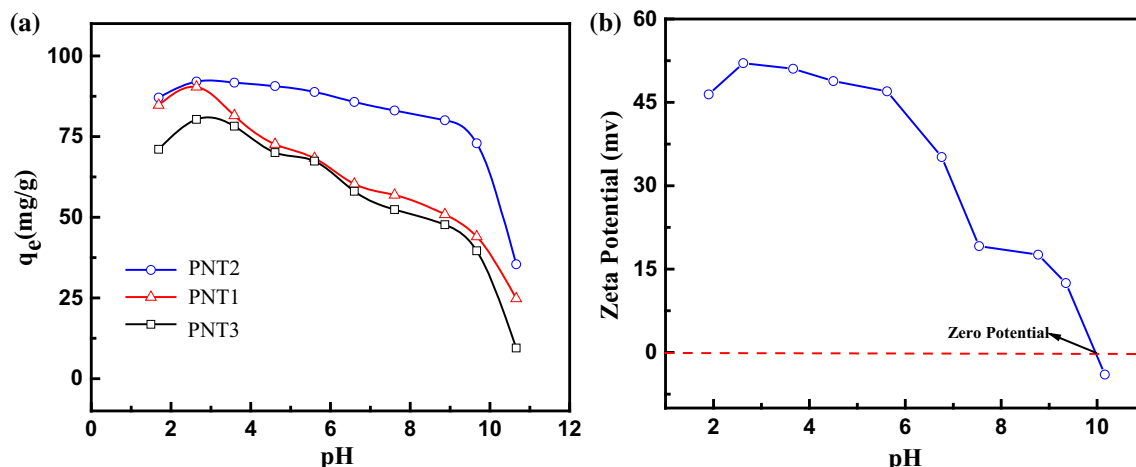


Figure 6 Effect of pH on adsorption of Cr(VI) (a) and Zeta potential of PNT2 (b).

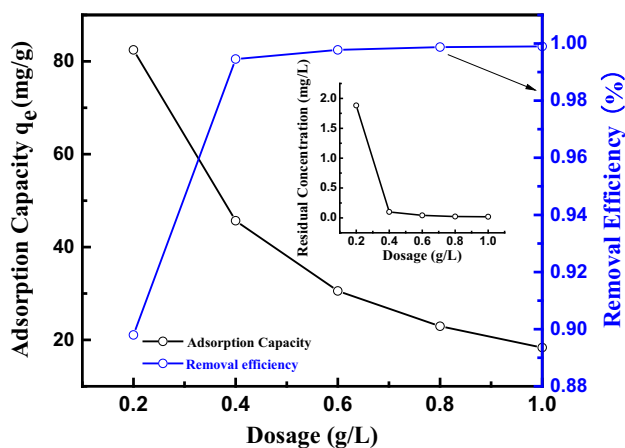


Figure 7 Effect of adsorbent dosage of PNT2.

rate. When the amount of adsorbent was only greater than 0.6 g L^{-1} in Cr(VI) solution (20 mg L^{-1}), the residual concentration of Cr(VI) could be less than the maximum allowable emission concentration (EPA, 0.05 mg L^{-1}) (Inserted Figure). The removal rate also was above 99% in 0.6 g L^{-1} adsorbent solution, while the adsorption capacity was reduced, which can be explained by the increase in available adsorption sites at a certain contaminant concentration [26]. In addition, an increase in the amount of adsorbent may increase the possibility of contact between adsorbents and cause aggregation. It also results in a reduction in mass-specific surface area. These two aspects led to a decrease in adsorption performance [27].

Adsorption kinetics

It is very important to investigate the adsorption mechanism by kinetics. Figure 8 shows the effect of adsorption time. In the first stage, the adsorption capacity of PNT2 increased rapidly and reached almost 90% in a short time. Then, its growth trend was gradually reduced and the adsorption eventually reached saturation. For the 20 mg L^{-1} solutions, the equilibrium adsorption capacity could be achieved in only 10 min. It was attributed to the pore structure of PNT2 and the chelating ability to metals by the functional groups of $-\text{NH}_2$ and $-\text{N}-$ [28]. In addition, the nanotube structures could provide more active sites. As the concentration of contaminants increases, the time required to reach equilibrium increased from 10 to 180 min. In the following work, the concentration of Cr(VI) did not exceed 140 mg L^{-1} , and the adsorption time is 180 min.

To further investigate the adsorption mechanism, the pseudo-first-order, pseudo-second-order, Elovich and intraparticle diffusion models were applied to evaluate kinetics data (Fig. 8b–e).

$$\text{Pseudo - first - order} \quad \ln[(q_e - q_t)/q_e] = -k_1 t \quad (3)$$

$$\text{Pseudo - second - order} \quad t/q_t = 1/(k_2 q_e^2) + t/q_e \quad (4)$$

$$\text{Elovich} \quad q_t = (1/\beta) \ln(\alpha\beta) + (1/\beta) \ln t \quad (5)$$

$$\text{Intraparticle diffusion} \quad q_t = k_d t^{1/2} + C \quad (6)$$

where the adsorption capacity is q_e (mg g^{-1}) at equilibrium. Pseudo-first-order constant was k_1 (min^{-1}). Pseudo-second-order and particle diffusion rate constants were k_2 ($\text{mg g}^{-1} \text{ min}^{-1}$) and k_d

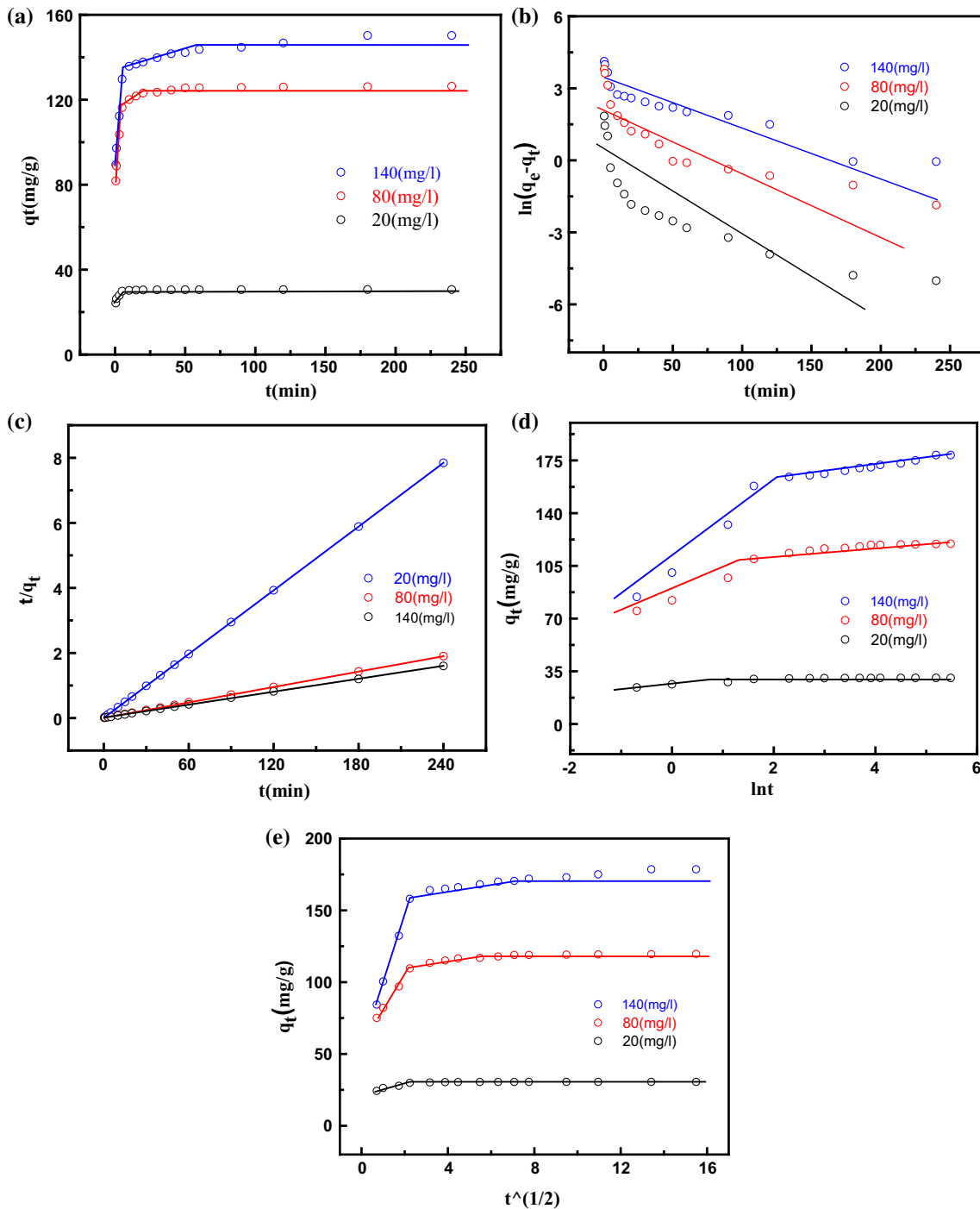


Figure 8 Effect of the contact time on the adsorption capacity Cr(VI) (a) and linear fits of pseudo-first-order (b), pseudo-second-order (c), Elovich (d), intraparticle diffusion (e) for Cr(VI) adsorption. (Dosage = 0.6 g L⁻¹, pH = 2.64.).

(mg g⁻¹ min^{1/2}), respectively. C represents the intraparticle diffusion constant.

These results are shown in Table 1. The decisive factor (R^2) was all above 0.999 in the pseudo-second-order, curves and it was far superior to the pseudo-

first-order and Elovich model. It indicated that the chemisorption was the rate-limiting step. It involved with valence forces by sharing or exchanging electrons of PNT2 and Cr(VI) [29]. The α value was much larger than the β value in the Elovich model. It

Table 1 Kinetic model parameters for Cr(VI) on PNT2

Kinetic model	Parameters	Cr(VI)			
		Initial concentration(mg L ⁻¹)			
		20	80	140	
Pseudo-first-order	q_e (mg g ⁻¹)	0.70	9.62	25.82	
	$k_1 \times 10^2$ (min ⁻¹)	2.48	2.05	1.59	
	R^2	0.6896	0.7101	0.8567	
Pseudo-second-order	q_e (mg g ⁻¹)	30.62	126.58	150.60	
	$k_2 \times 10^2$ (mg g ⁻¹ min ⁻¹)	21.20	1.49	0.39	
	R^2	0.9999	0.9999	0.9997	
Elovich	α_1 (mg g ⁻¹ min ⁻¹)	849.30	6209.80	269960.00	
	β_1 (mg g ⁻¹)	0.03	0.07	0.45	
	R^2	0.9841	0.9706	0.9456	
	α_2 (mg g ⁻¹ min ⁻¹)	3.19×10^{13}	9.34×10^{25}	4.61×10^{81}	
	β_2 (mg g ⁻¹)	0.19	0.53	6.36	
	R^2	0.7074	0.8449	0.7396	
		1st stage			
Interparticle diffusion	K_{d1} (mg g ⁻¹ min ^{1/2})	3.31	22.17	47.26	
	C_1	22.38	59.49	51.74	
	R^2	0.9349	0.9971	0.9977	
		2nd stage			
	K_{d2} (mg g ⁻¹ min ^{1/2})	0.19	1.71	1.75	
	C_2	29.55	107.50	158.42	
	R^2	0.8120	0.8675	0.9910	
		3th stage			
	$K_{d3} \times 10^2$ (mg g ⁻¹ min ^{1/2})	1.14	9.56	95.86	
	C_3	30.43	118.23	164.56	
R^2	0.8434	0.9905	0.9140		
$q_{e,exp}$ (mg g ⁻¹)		30.59	126.36	150.25	

implied that the adsorption was feasible and effective [30]. Then, we used Weber–Morris model to explore the adsorption rate control process (Fig. 8e). The order of adsorption rate was as follows:

$$K_{d1} > K_{d2} > K_{d3}$$

This order showed that the surface was gradually saturated with increasing time and the internal diffusion rate of Cr(VI) adsorbed gradually decreased. All values of C were not zero, implying that the diffusion mechanism could be affected by some other factors [31].

Adsorption isotherm

Five famous calculation formulae (Langmuir, Freundlich, Temkin, Langmuir–Freundlich, and Redlich–Peterson models) had been used to describe the isotherm at three different temperatures (Fig. 9).

$$\text{Langmuir } q_e = q_m K_L C_e / (1 + K_L C_e) \quad (7)$$

$$\text{Freundlich } q_e = K_F C_e^{1/n} \quad (8)$$

$$\text{Temkin } q_e = B(\ln K_T C_e) \quad (9)$$

$$\text{Langmuir – Freundlich } q_e = q_m (K_{LF} C_e)^n / [1 + (K_{LF} C_e)^n] \quad (10)$$

$$\text{Redlich – Peterson } K_R C_e / (1 + \alpha_R C_e^\beta) \quad (11)$$

$$\text{APE\%} = \sum_{i=1}^n |(q_{e,exp} - q_{e,cal}) / q_{e,exp}| \times 100 / N \quad (12)$$

where the Langmuir constant is K_L (L mg⁻¹). Freundlich constants contain K_F (mg g⁻¹), and n the Temkin constants are K_T (L mg⁻¹) and B ($B = RT/bT$). K_{LF} is the affinity constant [(mg g⁻¹) (L mg⁻¹)^{1/n}], and n is known as the heterogeneity index. α_R (mg⁻¹) and K_R (L g⁻¹) are the Redlich–Peterson constants. APE% is the average percent error.

Table 2 shows the isotherm parameters. The values of the Redlich–Peterson model were above 0.99, and

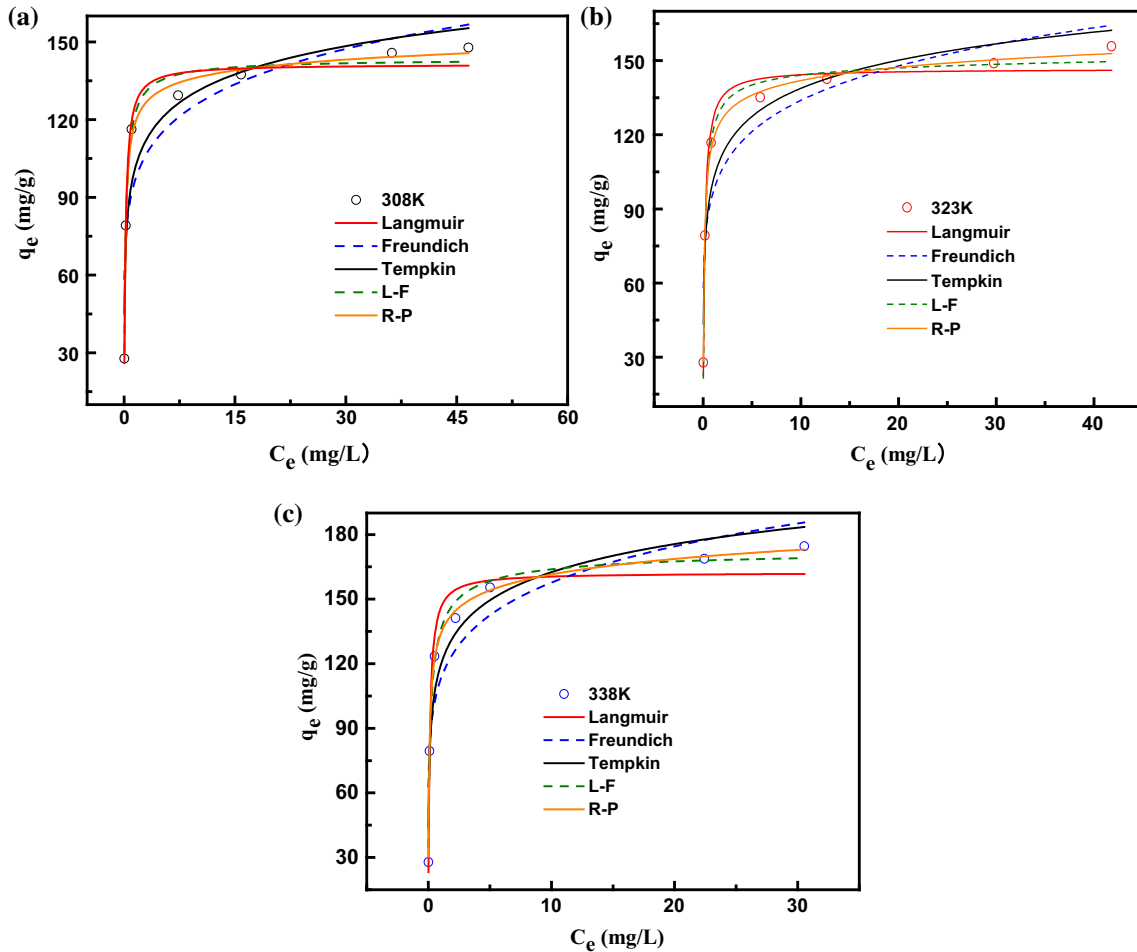


Figure 9 Nonlinear fits of isotherm models at different temperatures [308 K (a), 323 K (b), 338 K (c)]. (Dosage = 0.6 g L⁻¹, pH = 2.64, Contact time = 6 h.).

all the APE% of Redlich–Peterson models were the lowest in the five models. It was not difficult to observe that the Redlich–Peterson model was closer to the experimental data than the Langmuir, Freundlich, Temkin, and Langmuir–Freundlich equations. In Redlich–Peterson, the *g* values were 0.9642, 0.9539, and 0.9442 at the three temperatures. They were very close to 1, indicating that Redlich–Peterson was similar to the Langmuir model in this work [32]. In other words, it was monolayer adsorption and the monolayer uptake could reach 140.82 mg g⁻¹ and the binding constant was 5.30 L mg⁻¹ at 35 °C. The value of *q_m* was larger than that of many other adsorbents (Table 3), indicating that PNT2 could effectively adsorb the heavy metal of Cr(VI).

Thermodynamics parameters

The standard parameters [Gibbs free energy (ΔG°), enthalpy (ΔH°), and entropy (ΔS°)] could be calculated by the following equation.

$$K_c = q_e/C_e \tag{13}$$

$$\Delta G^\circ = -RT \ln K_c \tag{14}$$

$$\ln K_c = -\Delta H^\circ/RT + \Delta S^\circ/R \tag{15}$$

$$\Delta G^\circ = \Delta H^\circ - T\Delta S^\circ \tag{16}$$

where the universal gas constant is *R* [J/(mol K)], *K_c* (L g⁻¹) is the distribution coefficient in the ideal solution at a different temperature, and *T* (K) is the temperature of the solution.

Table 4 shows the resulting thermodynamic parameter of ΔG° , ΔH° , and ΔS° values for the adsorption. All the values of ΔG° were below zero, indicating that it was a spontaneous adsorption

Table 2 Isotherm parameters for Cr(VI) adsorption on PNT2

Isotherm models	T (K)	Parameter-1	Parameter-2	Parameter-3	R^2	APE %
Langmuir		q_m (mg g ⁻¹)	K_L (L mg ⁻¹)	$q_{e,cal}$ (mg g ⁻¹)		
	308	147.81	5.32	140.82	0.9828	3.86
	323	155.78	6.69	146.13	0.9790	5.25
	338	174.54	8.77	161.69	0.9619	7.77
Freundlich		K_F (mg g ⁻¹)	n			
	308	91.37	7.12		0.8156	22.39
	323	96.30	6.99		0.8375	22.21
	338	112.61	6.84		0.8398	24.96
Temkin		K_T (mg g ⁻¹)	B			
	308	422.45	15.70		0.9062	14.62
	323	467.94	16.42		0.9869	13.24
	338	556.48	18.84		0.9827	14.08
Langmuir–Freundlich		q_m (mg g ⁻¹)	K_{LF} (L mg ⁻¹)	n		
	308	143.63	5.09	0.86	0.9829	7.49
	323	151.33	5.56	0.76	0.9869	12.74
	338	174.07	6.55	0.66	0.9827	22.72
Redlich–Peterson		α_R (L g ⁻¹)	K_R (L mg ⁻¹)	g		
	308	967.95	7.59	0.96	0.9932	2.85
	323	1279.54	9.91	0.95	0.9971	1.48
	338	2183.81	15.33	0.94	0.9974	2.47

Table 3 Adsorption capacities of different sorbents for Cr(VI)

Adsorbents	pH	q_{max} (mg·g ⁻¹)	T (K)	References
Poly(MAAcH)-cl-EGDMA	4.0	93.66	308	[33]
Ch/Fe-CNF/PVA	5.2	80.00	303	[34]
Iron and lanthanum mixed oxyhydroxide-engraved chitosan	2.0	106.04	303	[35]
PPAS	2.0	111.11	298	[36]
Montmorillonite-supported magnetite nanoparticles	2.5	20.16	298	[37]
Reticulated chitosan	4.0	68.90	298	[38]
PNT2	2.64	147.81	308	In this work

Table 4 Thermodynamic parameter for Cr(VI) adsorption on PNT2

T (K)	ΔG° (kJ mol ⁻¹)	ΔH° (kJ mol ⁻¹)	ΔS° (J mol ⁻¹ K ⁻¹)
308	- 19.46	23.09	128.69
323	- 20.67		
338	- 21.94		

process. It was obvious that with the increase in temperature, the value of ΔG° was more negative. It implied that the high temperature was beneficial to spontaneous adsorption in this work. In addition, all the values of ΔH° were above 0, indicating that the adsorption was an endothermic process. The ΔS° also showed that PNT2 had a strong attraction to Cr(VI) and the adsorption was almost irreversible [39].

According to the thermodynamic parameters of ΔG° , it can be used to judge whether the process is a physical process or a chemical process to a certain extent. In general, the adsorption process was physical ($- 20 \text{ kJ mol}^{-1} < \Delta G^\circ < 0 \text{ kJ mol}^{-1}$) or chemisorption ($- 400 \text{ kJ mol}^{-1} < \Delta G^\circ < - 80 \text{ kJ mol}^{-1}$) [40]. It could be seen obviously that all the values ΔG° were about $- 20 \text{ kJ mol}^{-1}$ in this work, implying that physical adsorption was the main process.

Effect of coexisting ions

The surface of PNT2 and the electric double layer structure could be affected by the coexisting ions [41]. It can also seriously affect the removal rate of contaminants. Therefore, it is very necessary to explore

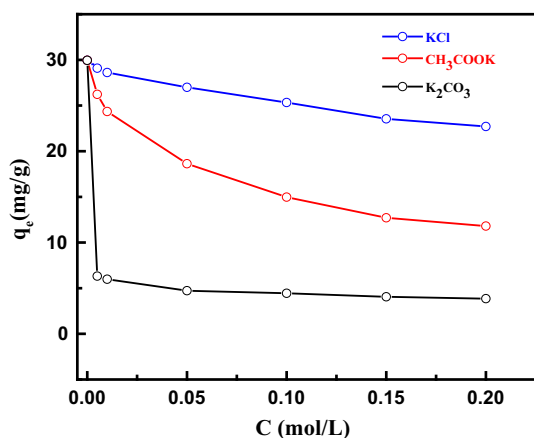


Figure 10 Effect of coexisting ions on the adsorption capacity.

the effect of coexisting ions on adsorption performance.

The concentration of coexisting ions increased from 0.01 to 0.2 M. The adsorption capacity was down (Fig. 10). It could be the following factors. (1) As the concentration of Cl^- , CH_3COO^- , and CO_3^{2-} increases, the adsorption sites could be consumed by electrostatic forces. (2) The HCrO_4^- was neutralized by K^+ [26]. The effect of coexisting ions was as follows: $\text{CO}_3^{2-} > \text{CH}_3\text{COO}^- > \text{Cl}^-$

First, the coexisting ions with a high negative charge had the greatest hindrance to adsorb Cr(VI). Second, coexisting ions with a large hydrated radius also had a large hindrance in the adsorption process.

Reusability test

Cyclic utilization is critical to actual production, and we used three different desorption solvents (NaOH solution, $\text{CH}_3\text{CH}_2\text{OH}$, and CH_3COCH_3) to measure the cyclic adsorption capacity of PNT2. The result is shown in Fig. 11.

NaOH solution was used as a desorption agent. The removal rate could be reached 99% after five cycles. However, ethanol and acetone were used as desorption agents. The removal rate decreased drastically after the second cycle. According to the polarity of the solvent (NaOH solution > ethanol > acetone) and similar compatibility principle, it could easy understand the order of desorption performance (NaOH solution > ethanol > acetone). Therefore, PNT2 had excellent regeneration and reusability capacities.

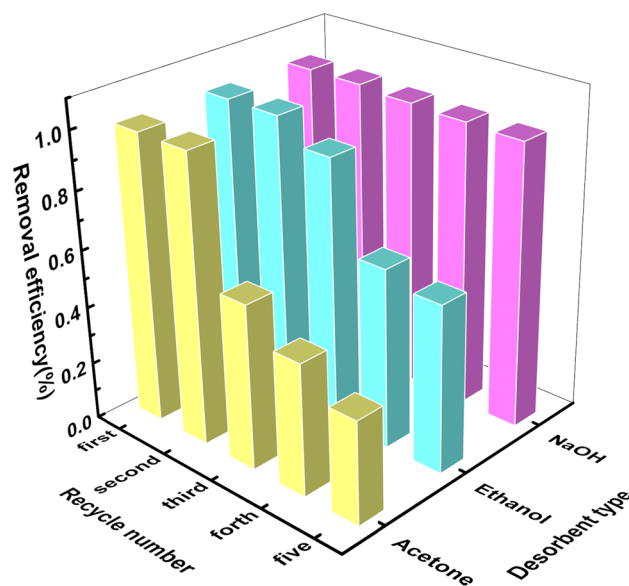


Figure 11 Reusability of the PNT2 using three different desorption solutions.

Adsorption mechanism

To further investigate the adsorption mechanism, we carried out EDS, mapping, and XPS on PNT2-Cr (after adsorption). The mapping and EDS showed that the element of Cr was enriched onto the nanotube surface of PNT2. The spectrum of Cr 2p contained two major bands, all of which can be divided into two small peaks (Fig. 12). The bands at 586.4 and 576.8 eV were due to the $\text{Cr}2p^{1/2}$ and $\text{Cr}2p^{3/2}$ of Cr(III), respectively. The bands at 588.6 and 579.9 eV were assigned to the $\text{Cr}2p^{1/2}$ and $\text{Cr}2p^{3/2}$ of Cr(VI), respectively. It indicated that the surface of PNT2 included both Cr(III) and Cr(VI) after adsorption. Cr(VI) had been reduced to Cr(III) by the functional groups ($-\text{NH}_2$ and $-\text{N}-$) during the adsorption process [17]. Above all, the Cr(VI) adsorption on PNT2 could be as follows. (1) The static electricity exists between the functional groups and Cr(VI). (2) The reduction and chelation also played a role by the functional groups of $-\text{NH}_2$ and $-\text{N}-$.

Conclusion

In this work, the nanotubes were successfully prepared by a simple Friedel–crafts alkylation process. The special structure could effectively remove Cr(VI) from the water. The maximum value of q_e was 140.82 mg g^{-1} in 140 mg L^{-1} Cr(VI) solution. Both

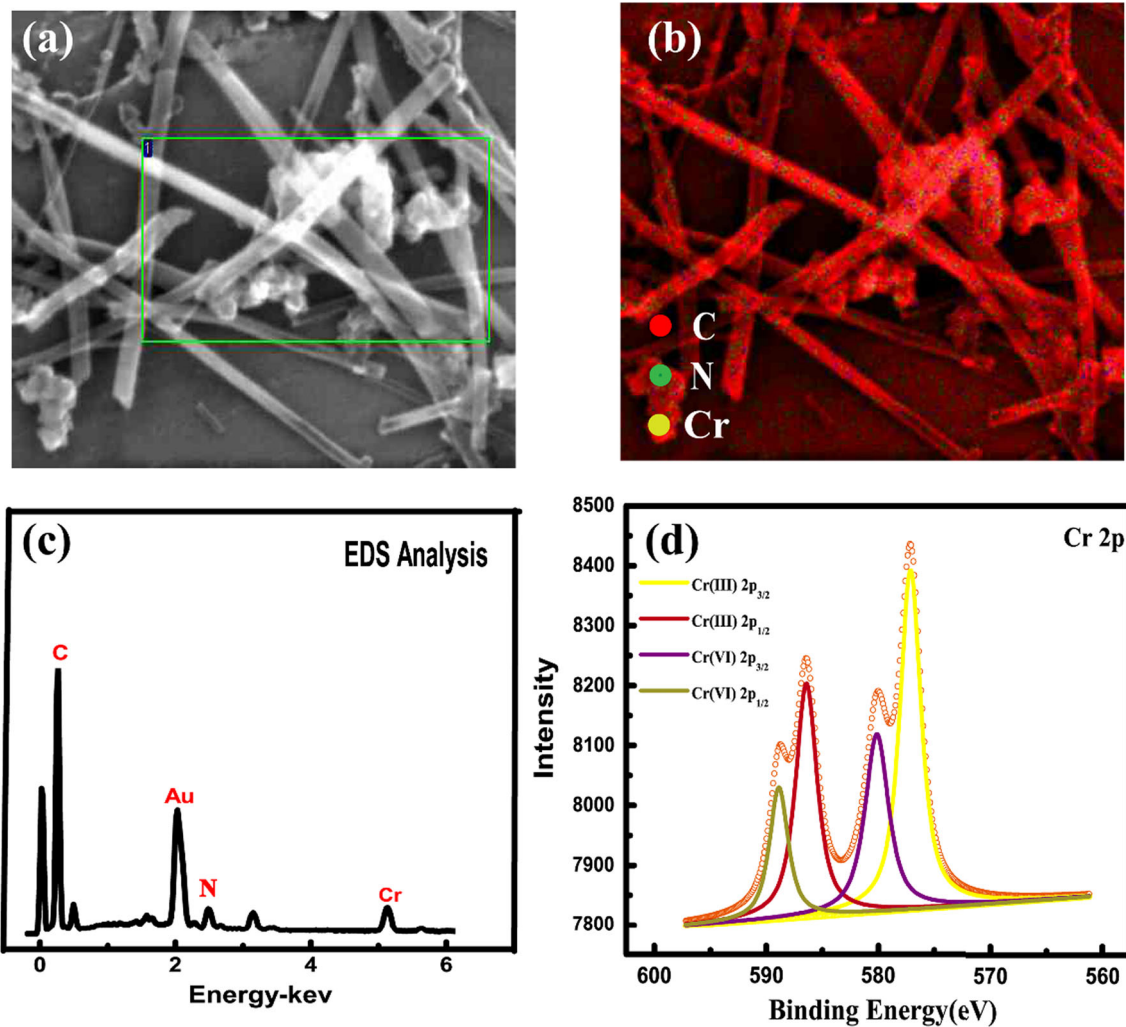


Figure 12 Microscopic morphology of PNT2 (a), mapping of PNT2 (b), EDS of PNT2 (c), and XPS of Cr 2p spectrum (d).

pH and coexisting ions had a huge impact on the adsorption performance. The adsorption was a spontaneous process, and the main adsorption mechanism was electrostatic interaction. This new material with an ordered structure could provide a new approach to remove the contaminant from water.

Acknowledgements

The authors are grateful to the Applied Basic Research Programs of Science and Technology Department of Sichuan Province (2018JY0115), the Application Technology Research and Development Special Project of Nanchong, China (18YFZJ0035), the Meritocracy Research Funds of China West Normal University (17YC013, 17YC139), and the Open Fund

of Sichuan Key Laboratory of Chemical Synthesis and Pollution Control (No. CSPC2015-6-2).

Compliance with ethical standards

Conflict of interest The authors declare that they have no conflict of interest.

References

- [1] Wu Y, Pang H, Liu Y et al (2019) Environmental remediation of heavy metal ions by novel-nanomaterials: a review. *Environ Pollut* 246:608–620. <https://doi.org/10.1016/j.envpol.2018.12.076>
- [2] Valentín-Reyes J, García-Reyes RB, García-González A, Soto-Regalado E, Cerino-Córdova F (2019) Adsorption mechanisms of hexavalent chromium from aqueous solutions on modified activated carbon. *J Environ Manag*

- 236:815–822. <https://doi.org/10.1016/j.jenvman.2019.02.014>
- [3] Zheng W, An Q, Lei Z, Xiao Z, Zhai S, Liu Q (2016) Efficient batch and column removal of Cr(VI) by carbon beads with developed nano-network. *RSC Adv* 6:104897–104910. <https://doi.org/10.1039/c6ra14070j>
- [4] Vakili M, Deng S, Li T, Wang W, Wang W, Yu G (2018) Novel crosslinked chitosan for enhanced adsorption of hexavalent chromium in acidic solution. *Chem Eng J* 347:782–790. <https://doi.org/10.1016/j.cej.2018.04.181>
- [5] Khan SU, Islam DT, Farooqi IH, Ayub S, Basheer F (2019) Hexavalent chromium removal in an electrocoagulation column reactor: process optimization using CCD, adsorption kinetics and pH modulated sludge formation. *Process Saf Environ Prot* 122:118–130. <https://doi.org/10.1016/j.psep.2018.11.024>
- [6] Zhang L, Xia W, Liu X, Zhang W (2015) Synthesis of titanium cross-linked chitosan composite for efficient adsorption and detoxification of hexavalent chromium from water. *J Mater Chem A* 3:331–340. <https://doi.org/10.1039/c4ta05194g>
- [7] GilPavas E, Dobrosz-Gómez I, Gómez-García M-Á (2019) Optimization and toxicity assessment of a combined electrocoagulation, $H_2O_2/Fe^{2+}/UV$ and activated carbon adsorption for textile wastewater treatment. *Sci Total Environ* 651:551–560. <https://doi.org/10.1016/j.scitotenv.2018.09.125>
- [8] Ge G, Yuanlai X, Xinxin Y et al (2017) Effect of HNO_3 concentration on a novel silica-based adsorbent for separating Pd(II) from simulated high level liquid waste. *Sci Rep* 7:1–9. <https://doi.org/10.1038/s41598-017-11879-6>
- [9] Zheng X, Yu N, Wang X et al (2018) Adsorption properties of granular activated carbon-supported titanium dioxide particles for dyes and copper ions. *Sci Rep* 8:6463. <https://doi.org/10.1038/s41598-018-24891-1>
- [10] Peng X, Gao F, Zhao J, Li J, Qu J, Fan H (2018) Self-assembly of a graphene oxide/ $MnFe_2O_4$ motor by coupling shear force with capillarity for removal of toxic heavy metals. *J Mater Chem A* 6:20861–20868. <https://doi.org/10.1039/c8ta06663a>
- [11] Shah LA, Khan M, Javed R et al (2018) Superabsorbent polymer hydrogels with good thermal and mechanical properties for removal of selected heavy metal ions. *J Clean Prod* 201:78–87. <https://doi.org/10.1016/j.jclepro.2018.08.035>
- [12] Zhan Y, He S, Wan X et al (2018) Easy-handling bamboo-like polypyrrole nanofibrous mats with high adsorption capacity for hexavalent chromium removal. *J Colloid Interface Sci* 529:385–395. <https://doi.org/10.1016/j.jcis.2018.06.033>
- [13] Ko D, Mines PD, Jakobsen MH, Yavuz CT, Hansen HCB, Andersen HR (2018) Disulfide polymer grafted porous carbon composites for heavy metal removal from stormwater runoff. *Chem Eng J* 348:685–692. <https://doi.org/10.1016/j.cej.2018.04.192>
- [14] Zhao G, Huang X, Tang Z, Huang Q, Niu F, Wang X (2018) Polymer-based nanocomposites for heavy metal ions removal from aqueous solution: a review. *Polym Chem* 9:3562–3582. <https://doi.org/10.1039/c8py00484f>
- [15] Tang WJ, Wu Y, Gao TT, Wei YQ, Zhou GW (2018) Facile preparation of hybrid porous polyanilines for highly efficient Cr(VI) removal. *RSC Adv* 8:33217–33227. <https://doi.org/10.1039/c8ra07026a>
- [16] Tu T, Assenmacher W, Peterlik H, Schnakenburg G, Dötz KH (2008) Pyridine-bridged benzimidazolium salts: synthesis, aggregation, and application as phase-transfer catalysts. *Angew Chem Int Ed* 47:7127–7131. <https://doi.org/10.1002/anie.200801628>
- [17] Yang Z, Ren L, Jin L et al (2018) In-situ functionalization of poly(m-phenylenediamine) nanoparticles on bacterial cellulose for chromium removal. *Chem Eng J* 344:441–452. <https://doi.org/10.1016/j.cej.2018.03.086>
- [18] Chen X, Huang Y, Zhang K, Feng X, Wang M (2017) Synthesis and high-performance of carbonaceous polypyrrole nanotubes coated with SnS_2 nanosheets anode materials for lithium ion batteries. *Chem Eng J* 330:470–479. <https://doi.org/10.1016/j.cej.2017.07.180>
- [19] Fellenz N, Perez-Alonso FJ, Martin PP et al (2017) Chromium (VI) removal from water by means of adsorption–reduction at the surface of amino-functionalized MCM-41 sorbents. *Microporous Mesoporous Mater* 239:138–146. <https://doi.org/10.1016/j.micromeso.2016.10.012>
- [20] Shao L, Wang S, Liu M, Huang J, Liu Y-N (2018) Triazine-based hyper-cross-linked polymers derived porous carbons for CO_2 capture. *Chem Eng J* 339:509–518. <https://doi.org/10.1016/j.cej.2018.01.145>
- [21] Li B, Guan Z, Wang W et al (2012) Highly dispersed Pd catalyst locked in knitting aryl network polymers for Suzuki–Miyaura coupling reactions of aryl chlorides in aqueous media. *Adv Mater* 24:3390–3395. <https://doi.org/10.1002/adma.201200804>
- [22] Balaban A, Dinculescu A, Elguero J, Faure R (1985) Carbon-13 NMR studies of primary amines and their corresponding 2,4,6-trimethyl-pyridinium salts. *Magn Reson Chem* 23:553–558
- [23] Xu C, Wang H, Wang Q, Wang Y, Zhang Y, Fan G (2019) Ruthenium coordinated with triphenylphosphine-hypercrosslinked polymer: an efficient catalyst for hydrogen evolution reaction and hydrolysis of ammonia borane. *Appl*

- Surf Sci 466:193–201. <https://doi.org/10.1016/j.apsusc.2018.10.051>
- [24] Zhang S, Wang X, Li J, Wen T, Xu J, Wang X (2014) Efficient removal of a typical dye and Cr(VI) reduction using N-doped magnetic porous carbon. RSC Adv 4:63110–63117. <https://doi.org/10.1039/C4RA10189H>
- [25] Sun X, Yang L, Xing H et al (2013) Synthesis of polyethylenimine-functionalized poly (glycidyl methacrylate) magnetic microspheres and their excellent Cr(VI) ion removal properties. Chem Eng J 234:338–345. <https://doi.org/10.1016/j.cej.2013.08.082>
- [26] Gao H, Du J, Liao Y (2019) Removal of chromium (VI) and orange II from aqueous solution using magnetic polyetherimide/sugarcane bagasse. Cellulose 26:3285–3297. <https://doi.org/10.1007/s10570-019-02301-7>
- [27] Huang J, Liu Y, Wang X (2008) Selective adsorption of tannin from flavonoids by organically modified attapulgite clay. J Hazard Mater 160:382–387. <https://doi.org/10.1016/j.jhazmat.2008.03.008>
- [28] Setyono D, Valiyaveetil S (2015) Functionalized paper—a readily accessible adsorbent for removal of dissolved heavy metal salts and nanoparticles from water. J Hazard Mater 302:120–128. <https://doi.org/10.1016/j.jhazmat.2015.09.046>
- [29] Du J, Zhang L, Gao H, Liao Y (2017) Removal of methylene blue from aqueous solutions using poly(AA-co-DVB). J Dispers Sci Technol 38:1489–1494. <https://doi.org/10.1080/01932691.2016.1255955>
- [30] Deng L, Shi Z, Wang L, Zhou S (2017) Fabrication of a novel NiFe₂O₄/Zn-Al layered double hydroxide intercalated with EDTA composite and its adsorption behavior for Cr(VI) from aqueous solution. J Phys Chem Solids 104:79–90. <https://doi.org/10.1016/j.jpcs.2016.12.030>
- [31] Liu X, Liao Y, Gao H (2018) Enhancement adsorption of hexavalent chromium from aqueous solution on polypyrrole using ethylamine group. J Dispers Sci Technol 39:1394–1402. <https://doi.org/10.1080/01932691.2017.1404917>
- [32] Terangpi P, Chakraborty S, Ray M (2018) Improved removal of hexavalent chromium from 10 mg/L solution by new micron sized polymer clusters of aniline formaldehyde condensate. Chem Eng J 350:599–607. <https://doi.org/10.1016/j.cej.2018.05.171>
- [33] Dautoo UK, Shandil Y, Chauhan GS (2017) New crosslinked hydrazide-based polymers as Cr(VI) ions adsorbents. J Environ Chem Eng 5:5815–5826. <https://doi.org/10.1016/j.jece.2017.10.041>
- [34] Khare P, Yadav A, Ramkumar J, Verma N (2016) Microchannel-embedded metal-carbon-polymer nanocomposite as a novel support for chitosan for efficient removal of hexavalent chromium from water under dynamic conditions. Chem Eng J 293:44–54. <https://doi.org/10.1016/j.cej.2016.02.049>
- [35] Preethi J, Vigneshwaran S, Meenakshi S (2019) Performance of chitosan engraved iron and lanthanum mixed oxyhydroxide for the detoxification of hexavalent chromium. Int J Biol Macromol 130:491–498. <https://doi.org/10.1016/j.ijbio mac.2019.02.101>
- [36] Rangabhashiyam S, Balasubramanian P (2018) Adsorption behaviors of hazardous methylene blue and hexavalent chromium on novel materials derived from *Pterospermum acerifolium* shells. J Mol Liq 254:433–445. <https://doi.org/10.1016/j.molliq.2018.01.131>
- [37] Mthombeni NH, Onyango MS, Aoyi O (2015) Adsorption of hexavalent chromium onto magnetic natural zeolite-polymer composite. J Taiwan Inst Chem Eng 50:242–251. <https://doi.org/10.1016/j.jtice.2014.12.037>
- [38] Kahu SS, Shekhawat A, Saravanan D, Jugade RM (2016) Two fold modified chitosan for enhanced adsorption of hexavalent chromium from simulated wastewater and industrial effluents. Carbohydr Polym 146:264–273. <https://doi.org/10.1016/j.carbpol.2016.03.041>
- [39] Zhang Y, Chen B, Zhang L et al (2011) Controlled assembly of Fe₃O₄ magnetic nanoparticles on graphene oxide. Nanoscale 3:1446–1450. <https://doi.org/10.1039/c0nr00776e>
- [40] Zhang L, Gao H, Liao Y (2016) Preparation and application of poly(AMPS-co-DVB) to remove Rhodamine B from aqueous solutions. React Funct Polym 104:53–61. <https://doi.org/10.1016/j.reactfunctpolym.2016.05.001>
- [41] Wang H, Yuan X, Wu Y et al (2015) Facile synthesis of polypyrrole decorated reduced graphene oxide-Fe₃O₄ magnetic composites and its application for the Cr(VI) removal. Chem Eng J 262:597–606. <https://doi.org/10.1016/j.cej.2014.10.020>

Publisher's Note Springer Nature remains neutral with regard to jurisdictional claims in published maps and institutional affiliations.